BIOCHEMISTRY
including biophysical chemistry & molecular biology

Article

pubs.acs.org/biochemistry

Specificity of the Double-Stranded RNA-Binding Domain from the RNA-Activated Protein Kinase PKR for Double-Stranded RNA: Insights from Thermodynamics and Small-Angle X-ray Scattering

Sunita Patel,[†] Joshua M. Blose,[‡] Joshua E. Sokoloski,[†,§] Lois Pollack,*[,‡] and Philip C. Bevilacqua*[,†]

[†]Department of Chemistry and Center for RNA Molecular Biology, The Pennsylvania State University, University Park, Pennsylvania 16802, United States

[‡]School of Applied and Engineering Physics, Cornell University, Ithaca, New York 14853, United States

Supporting Information

ABSTRACT: The interferon-inducible, double-stranded (ds) RNA-activated protein kinase (PKR) contains a dsRNA-binding domain (dsRBD) and plays key roles in viral pathogenesis and innate immunity. Activation of PKR is typically mediated by long dsRNA, and regulation of PKR is disfavored by most RNA imperfections, including bulges and internal loops. Herein, we combine isothermal titration calorimetry (ITC), electrophoretic mobility shift assays, and small-angle X-ray scattering (SAXS) to dissect the thermodynamic basis for the specificity of the dsRBD termed "p20" for various RNAs and to detect any RNA conformational changes induced upon protein binding. We monitor binding of p20 to chimeric duplexes containing terminal RNA−DNA hybrid segments and a central dsRNA segment, which was either unbulged ("perfect") or bulged. The ITC data reveal strong binding of p20 to the perfect duplex (K_d ∼ 30 nM) and weaker binding to the bulged duplex (K_d ∼ 2−5 μM). SAXS reconstructions and $p(r)$ distance distribution functions further uncover that p20 induces no significant conformational change in perfect dsRNA but largely straightens bulged dsRNA. Together, these observations support the dsRBD's ability to tightly bind to only A-form RNA and suggest that in a noninfected cell, PKR may be buffered via weak interactions with various bulged and looped RNAs, which it may straighten. This work suggests that PKR-regulating RNAs with complex secondary and tertiary structures likely mimic dsRNA and/or engage portions of PKR outside of the dsRBD.

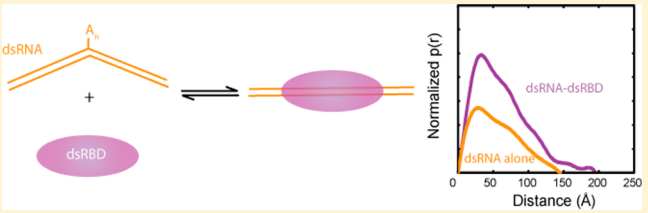

Protein kinase PKR is a key factor in innate immunity.[1] In the presence of long stretches of A-form dsRNA, PKR is activated to undergo autophosphorylation.[2,3] Once activated, PKR phosphorylates translation initiation factor eIF-2α, which blocks translation and thus pathogen replication. PKR consists of 551 amino acids and is comprised of an N-terminal dsRNA-binding domain (dsRBD), which has two tandem copies of the dsRNA-binding motif (dsRBM), and a C-terminal kinase domain. The dsRBM is a non-sequence-specific 65−70-amino acid RNA binding motif that has an $\alpha\beta\beta\beta\alpha$ secondary structure.[4−6] It binds non-sequence-specifically to A-form dsRNA primarily in its wide and shallow minor groove.[7−9] These interactions involve hydrogen bonds with the 2′-OH groups, which leads to discrimination against RNA−DNA hybrids.[7]

The dsRBM is present in many important proteins. For instance, Dicer and Drosha, which process highly structured miRNA precursors, have single copies of the dsRBM, as does *Escherichia coli* RNase III.[4−6] In addition, many proteins have multiple dsRBM copies, which are typically present in tandem: for example, PKR has two tandem copies of the dsRBM; the RNA-editing human adenosine deaminases (ADAR1 and ADAR2) have three and two copies, respectively; and the developmental protein Staufen has five tandem copies, with dsRBM3 and dsRBM4 being involved in dsRNA binding.[10−13]

While the dsRBM binds strongly to perfect dsRNA and also with varying degrees of affinity to dsRNAs with imperfections, it is not clear which RNAs activate PKR. This is an important issue as most cellular and viral RNAs are not perfectly double-stranded; for instance, pri- and pre-miRNAs contain helical defects,[14] as do most PKR regulators.[15] Studies from our lab and others support PKR binding to and being activated by RNA structures with bulges, hairpin loops, and pseudoknots, and by weakly structured RNAs with a 5′-triphosphate.[16−19] In at least several cases, the RNAs have complex folds that mimic A-form dsRNA.[16,19,20] In addition, ITC studies of PKR binding to the viral RNA inhibitors VAI RNA and EBER RNA, which have complex secondary and tertiary structures, have been conducted and have revealed tight and specific binding.[21−23]

We recently studied the interaction of PKR with model RNAs containing bulges and internal loops.[24] Bulges invariably decreased the level of PKR activation, although *trans*-bulges, in which flanking helices are on opposite sides of a central helix, inhibited activation more than *cis*-bulges, in which flanking helices are on the same side of a central helix. These studies

Received: July 13, 2012
Revised: October 21, 2012
Published: November 9, 2012

   dx.doi.org/10.1021/bi300935p | *Biochemistry* 2012, 51, 9312−9322

Chart 1

5′GGGAGAGGCAAGUCGUUCGGUCGCGUUCGC(A$_{0,3,6}$)UGUCGUCGCGUCUUGUAUGCCACUGUACCC3′ r(TSA$_{0,3,6}$)

3′CCCTCTCCGTTCAGCAAGCCAGCGCAAGCG------ACAGCAGCGCAGAACATACGGTGACATGGG5′ drd(BS)

extended earlier EMSA experiments, which had suggested that the dsRBM weakly interacts with a bulged RNA.[25]

In this study, we conduct thermodynamic and structural investigations of the binding of PKR and its N-terminal dsRBD, termed "p20", to various chimeric duplexes using EMSA, ITC, and SAXS. The chimeric duplexes contain a central, minimally sized dsRNA binding site flanked by RNA−DNA hybrid "arms". In addition, certain central segments are dsRNA with either A_3 or A_6 bulges, while others are purely RNA−DNA hybrids. We show that only the perfect dsRNA-containing chimeric duplex is capable of tightly binding the dsRBD from PKR, while all other sites bind weakly. We further find that p20 straightens bulged RNAs to a geometry consistent with A-form RNA. These findings suggest ways in which PKR may interact with biological RNAs that have complex secondary and tertiary structures.

MATERIALS AND METHODS

Expression and Purification of Proteins. The dsRBD of PKR, p20, and the full-length mutant K296R contained an N-terminal $(His)_6$ tag and were cloned as described previously.[7,17,25] Cells were sonicated, and the protein was purified by Ni^{2+}-agarose chromatography (Qiagen, Inc., Valencia, CA). Proteins were dialyzed into binding buffer (1×BB): 20 mM Hepes (pH 7.0), 200 mM sodium acetate, 0.1 mM EDTA, 5% glycerol, and 5 mM β-mercaptoethanol. The protein concentration was determined spectrophotometrically. The $(His)_6$ tag does not interfere with dsRNA affinity.[7]

Preparation of Oligonucleotides. DNA oligonucleotides were obtained from Integrated DNA Technologies (Coralville, IA) and the purity and length confirmed by denaturing polyacrylamide gel electrophoresis (PAGE) (Toluidine blue stain). For the bottom strands, the chimeric DNA22-RNA16-DNA22 60mer bottom strand, drd(BS), and an all-DNA version, d(BS), were purchased from IDT and purified by denaturing 10% PAGE, eluted by a crush and soak method, and concentrated by ethanol precipitation, as previously described.[18] Chimeric drd(BS) was 5′-radiolabeled by polynucleotide kinase and [γ-^{32}P]ATP. For the top strands, the three top-strand RNAs, termed r(TSA_0), r(TSA_3), and r(TSA_6), were studied. These were prepared by T7 transcription from a hemiduplex template and purified by denaturing 10% PAGE, a crush and soak method, and ethanol precipitation. RNA concentrations were determined spectrophotometrically using extinction coefficients calculated using nearest-neighbor parameters.

Duplexes were prepared by annealing a bottom strand with a top strand. Stoichiometric quantities of the two strands were used. Annealing occurred in 1×BB, heating at 95 °C for 3 min, and cooling at room temperature for 30 min. The sequences of the duplexes, in which RNA segments are underlined, are shown in Chart 1.

Electrophoretic Mobility Shift Assays (EMSAs). EMSAs were similar to those described previously,[7] except that the cross-linking was conducted with a 29:1 acrylamide:bisacrylamide ratio. The final temperature of the gel was maintained by a circulating water bath. Data were quantified on a Typhoon PhosphorImager using ImageQuant (Molecular Dynamics, Sunnyvale, CA).

Isothermal Titration Calorimetry (ITC). Binding of p20 to the chimeric duplexes was assessed by ITC (20 °C) using an AutoITC$_{200}$ (MicroCal, Inc., Northampton, MA). Solutions of p20 and chimeric duplexes were dialyzed overnight against 1×BB. The p20 concentration ranged from 100 to 300 μM, and p20 was titrated into 3−4 μM chimeric duplex solutions, whose concentrations were determined spectrophotometrically. Titrations consisted of 19 injections of 2 μL each, with a reference power of 5 μcal/s. Data were integrated and analyzed using Origin (OriginLabs, Inc., Northampton, MA). The background heat of dilution was corrected as follows. With one exception, the values of ΔH per mole of p20 for the last three injections were averaged and subtracted, as is fairly standard. The one exception was Figure 2B, in which the last five injections had not leveled off; here the heat of dilution for panel A, which is for the same duplex, was used for subtraction.

Sample Preparation and Data Collection for SAXS. SAXS samples of chimeric duplexes alone and p20 alone were prepared by diluting stocks (in 1×BB) with 1×BB to final concentrations of 10 and 30 μM, respectively, in a sample volume of 30 μL. The chimeric duplex−p20 complexes were prepared by addition of hybrid duplexes (in 1×BB) and p20 stocks (in 1×BB) and extra 1×BB as appropriate to concentrations of 10 μM duplex and 30 μM p20 in a 30 μL sample volume, matching concentration conditions of the gel shift assay from Figure 1. Duplexes and p20 were allowed to bind for 15 min prior to the collection of scattering data, which is sufficient for binding to come to equilibrium.[7]

SAXS data were collected at the Cornell High Energy Synchrotron Source (CHESS) G1 station at 10.5 keV. SAXS samples at ambient temperature (~20 °C) were loaded into a MacCHESS sample flow cell containing a 2 mm quartz capillary in vacuum, which allowed the sample to oscillate to avoid radiation damage.[26] Eight exposures (10 s each) were recorded using a fiber-coupled CCD[27] for each sample; images were normalized using the current from the beamstop PIN diode. Exposures from an individual sample were integrated and compared to ensure the absence of time-dependent changes that would indicate radiation damage of the sample. The scattering angle was converted to momentum transfer ($q = 4\pi \sin \theta/\lambda$, where 2θ is the scattering angle and λ is the X-ray wavelength) using a calibration based on scattering from a silver behenate standard.

Data Analysis and Reconstructions for SAXS. Scattering curves for each sample were averaged, background-subtracted, and concentration-scaled. Errors were propagated for each manipulation and used in subsequent fitting analysis. *GNOM*[28] was used to generate $p(r)$, the pairwise distance distribution function of the molecules, from the scattering data. *GNOM* outputs and scattering curves were subsequently supplied as input for reconstruction programs *DAMMIF*[29] [r(TSA_0)/drd(BS) alone and p20 alone] and *MONSA*[30] (complex). The output of at least 10 individual runs was averaged using *DAMAVER*[31] and then aligned with available NMR or other model structures using *SUPCOMB*[32] and subsequent small

dx.doi.org/10.1021/bi300935p | *Biochemistry* 2012, 51, 9312−9322

manual adjustments. All SAXS envelopes along with corresponding models were visualized using *PyMOL 1.5*[33] or *Accelrys Discovery Studio 3.1* (Accelrys, San Diego).

RESULTS

Rationale for the Design of the RNA−Protein System. Previous studies suggested that bulges interfere with PKR activation to various degrees. We wished to explore the thermodynamics of specificity of interaction of p20 with various nucleic acids, including perfect dsRNA, bulged dsRNA, and RNA−DNA hybrids in different contexts. A chimeric duplex was engineered in which a DNA−RNA−DNA bottom strand was annealed to various all-RNA top strands. The chimeric bottom strand, drd(BS), is a DNA22-RNA16-DNA22 60mer that when annealed to a 60mer complementary RNA, r(TSA_0), gives a duplex termed r(TSA_0)/drd(BS) containing an internal 16 bp dsRNA segment. We previously showed that 16 bp is the minimal length of dsRNA required to give a single gel shift with p20, and that 22 bp of dsRNA gives two gel shifts.[7] By flanking the minimally sized dsRNA segment with RNA−DNA hybrid arms, we hoped to be able to study specific and nonspecific interactions of p20 accurately in a single experimental run. Moreover, this chimeric duplex facilitated SAXS analysis as the greater number of phosphates provided increased scattering intensity on a per mole basis and provided for more pronounced changes in D_{Max} upon binding of p20 to the bulged hybrids.

EMSAs of the Chimeric Duplex Binding to p20 and K296R. In an effort to assess the stoichiometry and qualitative affinity of RNA−protein complex formation, EMSAs were conducted with full-length PKR or its dsRBD and the chimeric duplexes. These experiments provide insight into the affinity and stoichiometry of binding, and they guide sample preparation and building of binding models for ITC and SAXS studies. We first confirmed the formation of a duplex between p*drd(BS) (where p* denotes ^{32}P label) and various RNA top strands at 20 °C. As shown in Figure 1, the mobility of p*drd(BS) decreased as stoichiometric amounts (10 μM) of unlabeled RNA top strand were added (compare lane 1 to lanes 2−4), and the electrophoretic mobility of the duplex RNA species decreased further as the size of the bulge increased (in Figure 1, compare lanes 2−4), as expected.[34,35] Moreover, all of the p*drd(BS) shifted to a duplex, consistent with the proper stoichiometry.

Next, binding between the duplexes and p20 was assessed. Addition of 30 μM p20, which is in excess of the K_d from ITC (see below), led to loss of the majority of the free duplex for all three chimeras (in Figure 1, compare free duplex in lanes 2−4 to lanes 5−7), indicative of protein−nucleic acid interaction and supporting proper annealing of the duplex. In the case of the perfect chimeric duplex, r(TSA_0)/p*drd(BS), a single shifted band cleanly formed on the native gel (Figure 1, lane 5), while for the A_3- and A_6-bulged chimeric duplexes, additional shifted bands formed at higher mobilities, with some of the duplex forming a smear (Figure 1, lanes 5−7). Only a small amount of such smearing was observed for the perfect chimeric duplexes (Figure 1, top portion of lane 5), indicating that this was a good condition for SAXS reconstruction (see below). Overall, the observed EMSA behavior of all three chimeras is suggestive of a single specific complex, as expected from a minimal (16 bp) dsRNA binding site,[7] and approximately two additional weak nonspecific interactions with the RNA−DNA hybrids (see also below Figure S2A of the Supporting Information), as expected from 22 bp nonspecific sites.[7]

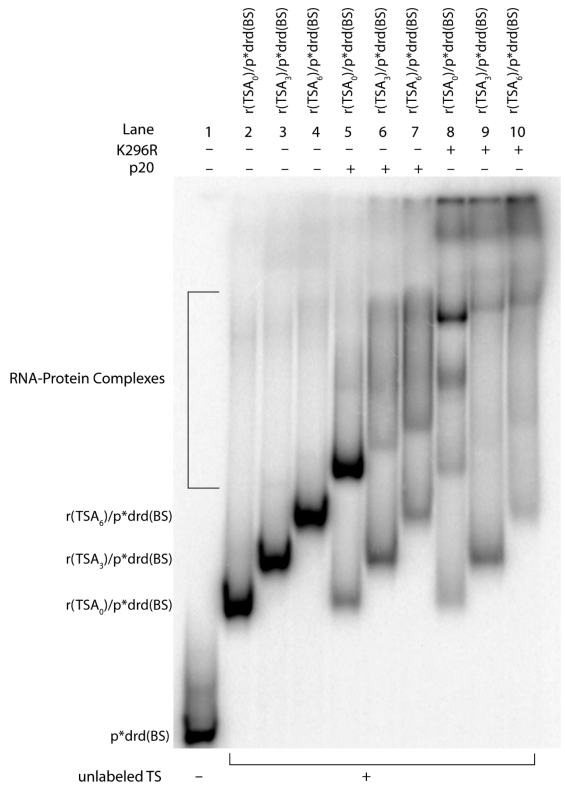

Figure 1. Binding of p20 and K296R to chimeric duplexes assessed by an EMSA. The bottom-strand (BS) chimeric oligonucleotide drd(BS) was 5′-^{32}P-labeled and annealed to equal amounts of unlabeled top-strand (TS) RNA oligonucleotides to afford a final duplex concentration of 10 μM. Formation of the chimeric duplex was confirmed by a shift of p*drd(BS) upon addition of unlabeled TS (compare lane 1 to lanes 2−4). p20 (lanes 5−7) or K296R (lanes 8−10) was added to a final concentration of 30 or 20 μM, respectively. These concentrations are relevant to the SAXS experiments described below. RNA−protein complexes formed as indicated. The temperature of the native gel conditions was maintained at 20 °C, the same as that in the ITC experiments.

We next consider EMSAs between the duplexes and the full-length PKR mutant, K296R, which is a version of PKR that has a mutation in the kinase domain.[1,36] Binding was overall similar to that observed with p20, with one cleanly shifted band for the perfect chimeric duplex of significantly slow mobility to likely account for one full-length PKR of 551 amino acids (Figure 1, lane 8), and smears for the A_3- and A_6-bulged chimeric duplexes that extend to the well (Figure 1, lanes 9 and 10). The band formed between the perfect chimeric duplex and K296R is not as well-defined as that formed with p20 (in Figure 1, compare lanes 5 and 8), and all chimeric duplexes led to samples in the well (Figure 1, lanes 8−10). Given the simpler behavior of p20 and our interest in elucidating the binding specificity of the dsRBM in general, we focused the remainder of the studies on p20.

In an effort to further assess specificity and affinity, EMSAs of p20 and perfect or bulged chimeric duplexes were conducted in the presence of nonspecific protein and DNA. Bovine serum albumin (BSA) (New England Biolabs) and herring sperm DNA (Sigma) were added to final concentrations of 20 and 100 μg/mL, respectively. These two nonspecific factors had little

dx.doi.org/10.1021/bi300935p | *Biochemistry* 2012, 51, 9312−9322

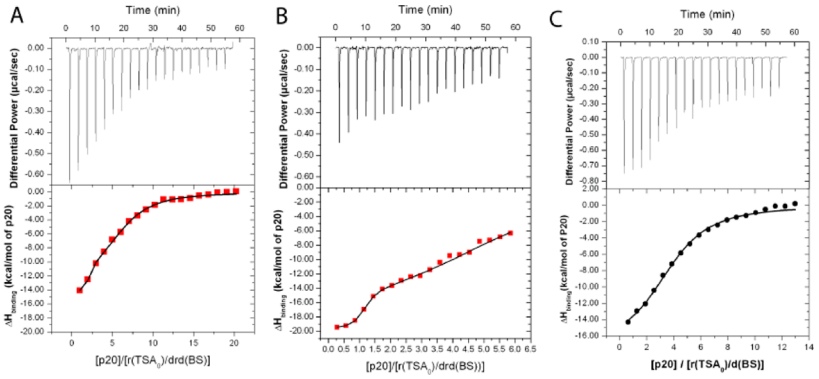

Figure 2. ITC reveals specific and nonspecific binding of p20 to the perfect chimeric duplex at 20 °C. Top panels show raw differential power vs time data for the calorimetric titrations (*x*-axis label at the top). Bottom panels show integrated injection heats vs the molar ratio of p20 to nucleic acid (*x*-axis label at the bottom); solid lines represent the fits of the data to the binding model. (A) Titration of 296 μM p20 into 2.98 μM r(TSA$_0$)/drd(BS) duplex. Data were fit to a two-classes-of-sites binding model. This corresponds to rows 1 and 3 of Table 1. (B) Titration of 115 μM p20 into 4.00 μM r(TSA$_0$)/drd(BS) chimeric duplex. In this concentration range, the specific tight site is observed clearly. Data were fit to a two-classes-of-sites binding model. This corresponds to rows 2 and 4 of Table 1. SAXS data were acquired at the 3:1 molar ratio where specific binding is still predominant. (C) Titration of 254.5 μM p20 into 4 μM r(TSA$_0$)/d(BS) control RNA–DNA hybrid duplex. Data were fit to a one-class-of-site binding model, and results are provided in row 5 of Table 1 (note that these symbols match in shape and color those in Figure 3).

Table 1. Thermodynamic Parameters for p20 Binding to Various Duplexes Obtained by ITC at 20 °C

	row	binding model[a]	site	mole ratio	*n*	K_d (μM)	ΔH^o (kcal/mol)	ΔS^o (eu)	Figure
strong sites[b]									
r(TSA$_0$)/drd(BS)	1	two-site	strong	0–20	1.6 ± 0.2	0.030 (fixed at row 2 value)	−14.3 ± 0.3	−14.4 ± 0.9	2A
r(TSA$_0$)/drd(BS)[c]	**2**	**two-site**	**strong**	**0–6**	**1.00 ± 0.06**	**0.030 ± 0.020**	**−19.6 ± 0.3**	**−32 ± 2**	2B
weak sites[b]									
r(TSA$_0$)/drd(BS)[c]	**3**	**two-site**	**weak**	**0–20**	**4.4 ± 0.2**	**3.5 ± 0.5**	**−13 ± 1**	**−21 ± 4**	2A
r(TSA$_0$)/drd(BS)	4	two-site	weak	0–6	4.6 ± 1	5 ± 1	−19 ± 2	−41 ± 7	2B
r(TSA$_0$)/d(BS)[d]	5	one-site		0–13	3.8 ± 0.1	3.2 ± 0.4	−17.5 ± 0.7	−35 ± 2	2C
r(TSA$_3$)/drd(BS)[d]	6	one-site		0–13	4.2 ± 0.1	2.0 ± 0.2	−14.7 ± 0.4	−24.0 ± 0.7	3A
average of weak sites[e]	7				4.1 ± 0.2	2.9 ± 0.7	−15.1 ± 1.3	−26.7 ± 4.5	

[a]All ITC data were fit with either a one- or two-site model; if the two-site model was used, the two binding events are separated in the table and the nature of the site, strong or weak, is indicated (rows 1 and 3 come from the same experiment, as do rows 2 and 4). Errors are from fits. [b]Strong or weak binding events are grouped. [c]Bold data are more reliable, because titrations focused data in the region of the transition. [d]Fit to one-site models; data were consistent with the weaker of the two r(TSA$_0$)/drd(BS) model sites. [e]Average of weak site binding data; data from row 4 are omitted from this average because they are less reliable.

effect on the EMSAs (Figure S1 of the Supporting Information, lanes 5–10), which supports structural specificity.

We then assessed whether decreasing the temperature from 20 to 10 °C affects the number of resolvable stable complexes. Low-temperature EMSAs with the perfect chimeric duplex led to resolved 1:1 and 2:1 complexes, and even ≥3:1 complexes were partly resolved at protein concentrations of >1 μM (Figure S2 of the Supporting Information), which approaches the K_d for nonspecific binding determined by ITC (see below). The observation of higher-stoichiometry complexes supports the notion that a dynamic component to the binding of the RNA–DNA segments can be minimized by lowering the temperature. At the highest concentrations of p20 (≥4 μM), only a smear with a highly retarded mobility was observed, which is diagnostic of nonspecific binding.

Low-temperature EMSAs were also conducted with the A$_6$-bulged chimeric duplex and led to formation of 1:1, 2:1, and ≥3:1 complexes (Figure S3 of the Supporting Information) in a fashion similar to that of the perfect chimeric duplex; however, somewhat more protein was required for the A$_6$-bulged duplex, and the 1:1 complex did not accumulate as it did with the perfect chimeric duplex (compare lane 8 of Figure S2 of the Supporting Information and lane 10 of Figure S3 of the Supporting Information). Overall, EMSAs at 10 °C support the binding model developed with 20 °C data described above (and below for SAXS), namely that p20 interacts tightly with a 16 bp dsRNA segment, less strongly with a bulged RNA segment, and nonspecifically with the 22 bp RNA–DNA hybrid arms.

ITC of Chimeric Duplexes Binding to p20. In an effort to measure the actual thermodynamic parameters in solution, binding between p20 and the perfect chimeric duplex was measured by ITC. These data revealed two distinct binding interactions as expected from the EMSA data and the construct design, which required fitting to a two-site model. As shown in Figure 2A, ∼20 equiv of protein was required to reach saturation. To provide more accurate data about the initial strong binding event, the 19-injection titration was repeated over a mole ratio of just 6 equiv of protein to duplex (Figure 2B). Table 1 provides the full core thermodynamic parameters for binding between p20 and r(TSA$_0$)/drd(BS). The first binding site has a $K_{d,1}$ of 30 ± 20 nM with an n_1 of 1.00 ± 0.06 sites (Table 1, row 2). The enthalpy of this first tight site is strongly favorable (ΔH^o_1 = −19.6 ± 0.3 kcal/mol), while the entropy is penalizing (ΔS^o_1 = −32 ± 2 eu). The second binding interaction has ∼170-fold weaker affinity than the first ($K_{d,2}$ = 5 ± 1 μM) and a much larger number of sites (n_2 = 4.6 ± 1)

dx.doi.org/10.1021/bi300935p | *Biochemistry* 2012, 51, 9312–9322

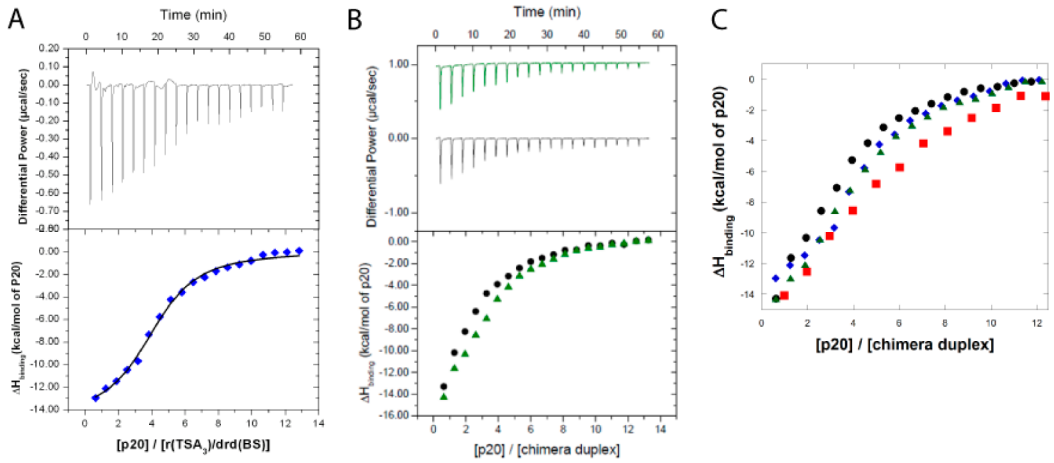

Figure 3. ITC reveals weak binding of p20 to the bulged chimeric duplexes at 20 °C. Top and bottom panels for A and B are as described in the legend of Figure 2. (A) Titration of 254.5 μM p20 into 4 μM r(TSA$_3$)/drd(BS). Data were fit to a one-class-of-site model, and results are listed in row 6 of Table 1. (B) Comparison of the titration of 254.5 μM p20 into 4 μM r(TSA$_6$)/drd(BS) (green trace in the top panel, green triangles in the bottom panel) with the titration of 254.5 μM p20 into 4 μM r(TSA$_0$)/d(BS) (black trace in the top panel, black circles in the bottom panel). (C) Comparison of calorimetric p20 binding curves for binding to r(TSA$_0$)/drd(BS) (red squares), r(TSA$_3$)/drd(BS) (blue diamonds), r(TSA$_6$)/drd(BS) (green triangles), and r(TSA$_0$)/d(BS) (black circles) (note that these symbols match in shape and color those in Figure 2).

(Table 1, row 4). The enthalpy for the weak sites is similar to that for the first tight site, with a ΔH°_2 of -19 ± 2 kcal/mol.

Next we consider the weaker sites in more detail. Full saturation data were examined for p20 and r(TSA$_0$)/drd(BS) to a mole ratio of 20 (Figure 2A), in which the binding constant for the first interaction was fixed to the values determined over the above, narrower titration. This provided an n_2 of 4.4 ± 0.2 sites for the weak nonspecific interaction, with a $K_{d,2}$ of 3.5 ± 0.5 μM (Table 1, row 3). The enthalpy of the second site (ΔH°_2) is -13 ± 1 kcal/mol, and the entropy (ΔS°_2) is -21 ± 4 eu. These values are somewhat different from those of the weak sites for the low-mole ratio data (in Table 1, compare rows 3 and 4), but the affinity, stoichiometry, and enthalpically driven nature of the binding are similar. Overall, the most reliable thermodynamic data for the tight site come from the 0–6 mole ratio titration (Table 1, row 2) and for the weak sites from the 0–20 mole ratio titration (Table 1, row 3), because more data are provided in key regions for each of these two titrations.

To provide a comparison to the chimeric portion of the duplex arms, the binding of p20 to a full RNA–DNA hybrid was tested by ITC. These data could be well fit to a one-site model, which is as expected based upon the homogeneity of the hybrid duplex structure, as compared to the dual-site nature of the r(TSA$_0$)/drd(BS) chimeric duplex (Figure 2C). We also attempted to fit the full RNA–DNA hybrid data set to a two-sets-of-sites model like that used with the chimeric duplex; however, this did not fit the data well, as determined by the fit errors and the χ^2 divided degrees of freedom parameter. One possible issue may be that apparent binding affinities are decreasing with near saturation of the chimera, as expected for nonspecific interactions, leading to the observed heats for the last three injections being slightly lower than the modeled values (e.g., see the last three data points in Figures 2A,C and 3A). However, the very low magnitude of the heats for these last three injections precluded our ability to fit these data to a more complex mechanism such as the McGhee–von Hippel model.[37] Because these very minor deviations are only for the last three of 19 injections, they are unlikely to cause large errors in the thermodynamic parameters. These and all subsequent titrations were conducted at a mole ratio of ~13, which is intermediate between the mole ratio limits tested with the perfect chimeric duplex. The interaction between p20 and r(TSA$_0$)/d(BS) was similar to that for the weak binding interaction in the perfect chimeric duplex, with similar n, K_d, ΔH°, and ΔS° thermodynamic parameters (in Table 1, compare rows 3 and 5). Although this is the first report of an RNA–DNA hybrid binding to PKR of which we are aware, weak binding of RNA–DNA hybrids has been reported previously for *Xenopus* 4F protein, which contains two tandem dsRBMs.[38] It appears that this interaction cannot be resolved by direct shifting with EMSAs (Figure 1, lane 5, and earlier studies[7]) and can barely be detected in a competition EMSA.[7]

The interaction between p20 and A$_3$- and A$_6$-bulged chimeric duplexes was also investigated via ITC and the A$_3$ data could be fit to a one-site model as shown in Figure 3A. The fit is good, with the possible exception of very minor deviations in the last three points; as discussed above, this could be due to near saturation of the chimera but is unlikely to cause significant error in the thermodynamic parameters. Binding parameters of the A$_3$-bulged duplex, r(TSA$_3$)/drd(BS), were similar to those of the weak binding interaction in the perfect chimeric duplex (in Table 1, compare rows 3, 5, and 6).

Interaction between p20 and the A$_6$-bulged duplex, r(TSA$_6$)/drd(BS), could also be detected. The A$_6$-bulged chimeric data could not be fit reliably to one- or two-class-of-sites models, so we turned to comparison of the raw heat released for related duplexes under identical experimental conditions (i.e., same temperature and same duplex and protein concentrations). Binding of p20 to the A$_6$-bulged duplex gave slightly greater exothermic heats per injection than binding to the RNA–DNA hybrid (in Figure 3B, compare triangles to circles); this indicates that p20 interacts more strongly with the A$_6$-bulged duplex than the control RNA–DNA hybrid. At the same time, binding of p20 to both A$_3$- and A$_6$-bulged chimeric duplexes was less exothermic than binding to the perfect chimeric duplex (in Figure 3C, compare diamonds and triangles to squares), although that binding was more exothermic than that of just the RNA–DNA hybrid (in Figure 3C, compare to circles), suggestive of recognition of the 2′-OH, even in the context

dx.doi.org/10.1021/bi300935p | *Biochemistry* 2012, 51, 9312–9322

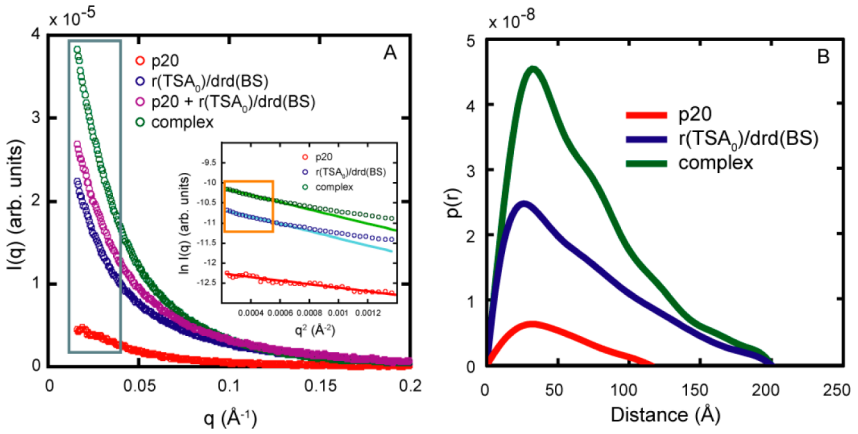

Figure 4. Scattering profiles and $p(r)$ for p20, r(TSA$_0$)/drd(BS), and their complex. (A) Scattering intensity of p20 (red), r(TSA$_0$)/drd(BS) (blue), the sum of the two curves (purple), and the complex (green). The complex scattering (green curve) has been corrected for ∼20 μM free p20. Note that the hybrid duplex scattering (blue) is significantly greater than that of p20 (red) because of the increased electron density of the nucleic acid even though the concentration of p20 is 3 times that of the duplex (the ratio for complex formation). Also, the sum (purple) of p20 (red) and r(TSA$_0$)/drd(BS) (blue) is not the same as the complex curve (green), supporting that the complex has formed. Error bars are not shown, as they are smaller than the data points (∼1%). A log−log plot of these data is provided in Figure S5 of the Supporting Information. The area enclosed by a gray box highlights the data shown in the Guinier plot inset. R_g is computed from data in the Guinier regime (qR_g < 1.3), within the orange box in the inset. (B) $p(r)$ plot for p20, r(TSA$_0$)/drd(BS), and the complex, colored as in panel A generated from *GNOM*. The data are scaled as in panel A. The 200 Å $p(r)$ curve is shown for both the duplex and the complex.

of bulges; this latter point is important for modeling of the scattering data (see below). Next we turned to SAXS to examine the conformations of p20, the chimeric duplexes, and their complexes.

SAXS Scattering Profiles and Pairwise Distribution Functions for Chimeric Duplexes and p20, Alone and in a Complex. SAXS studies have been previously conducted on PKR for full-length protein in the absence of RNA, where the data were consistent with the linkers between the dsRBMs and between the dsRBD and the kinase domain being flexible.[39] In an effort to gain insight into RNA conformational changes and the dsRBD in general, we conduct SAXS here on the dsRBD alone, on the chimeric duplexes alone, and on the various complexes.

Scattering profiles of r(TSA$_0$)/drd(BS), p20, and their complex are provided in Figure 4. The concentrations of free protein (red curve) and nucleic acid (blue curve) are the same as their concentrations in the final complex solution, 30 and 10 μM, respectively. The complex scattering (green curve) has been corrected for ∼20 μM free p20, although this correction is minor as the duplex dominates the scattering. The sum of the scattering of the duplex and p20 (purple curve) is not equivalent to the scattering of the complex (green curve), which suggests that the bound complex has formed and that the data are not simply monitoring the free species in solution. In addition, a Guinier plot of the data (Figure 4, inset) reveals the lack of an upturn at low q values, which supports minimal aggregation in the sample.

GNOM analysis of the data was performed at q values of up to ∼0.15 Å^{-1}; higher q values were omitted to avoid utilizing low signal-to-background data. D_{Max} was systematically varied until changes in D_{Max} that yielded a good fit to the data did not significantly change the shape of $p(r)$. D_{Max} and R_g for all species are listed in Table 2. Figure 4B shows the *GNOM*-generated $p(r)$ for D_{Max} scales used in reconstructions for p20 alone (red curve), r(TSA$_0$)/drd(BS) alone (blue curve), and the complex (green curve). The D_{Max} for p20 from the $p(r)$ is 115 Å. This distance is reasonable based on the NMR structure

Table 2. Structural Parameters from Analysis of SAXS Data for Components and Complexes

species	$R_{g(Guinier)}$ (Å)	$R_{g(GNOM)}$ (Å)	D_{Max} (Å)
	Components		
r(TSA$_0$)/drd(BS)	52.4 ± 0.3	55.4 ± 0.2	200
r(TSA$_3$)/drd(BS)	46.9 ± 0.4	49.6 ± 0.2	180
r(TSA$_6$)/drd(BS)	44.3 ± 0.3	44.4 ± 0.1	145
p20	35.6 ± 0.5	37.2 ± 0.2	115
	Complexes		
r(TSA$_0$)/drd(BS)−p20	52.1 ± 0.2	54.1 ± 0.2	200
r(TSA$_3$)/drd(BS)−p20	48.8 ± 0.3	51.2 ± 0.2	195
r(TSA$_6$)/drd(BS)−p20	48.4 ± 0.2	49.9 ± 0.2	195

of p20 (Protein Data Bank entry 1QU6),[40] where the longest distance ranges from ∼105 to 115 Å depending on the NMR conformer chosen; more than 50% of the NMR conformers have a longest distance of ≥110 Å.

For the r(TSA$_0$)/drd(BS) chimeric duplex, reasonable $p(r)$ values were found, with D_{Max} values between 195 and 200 Å, which did not significantly change the shape of the pairwise distribution (data not shown). These D_{Max} values are longer than what would be predicted for a cylindrical model of an A-form helix (176 Å) but shorter than what would be predicted for a B-form helix (205 Å), assuming helical diameters of 23 and 20 Å and representative rises per base pair of 2.9 and 3.4 Å, respectively. The literature has suggested that RNA−DNA hybrids can adopt a range of helical conformations,[41,42] with many helices displaying characteristics between the extremes of A- and B-form helices. It is not surprising, therefore, that r(TSA$_0$)/drd(BS) possesses intermediate characteristics. Interestingly, if the RNA−DNA regions were treated as B-form (44 bp), and the RNA−RNA region (16 bp) were treated as A-form, using either helical radius, the D_{Max} would be ∼197 Å, which is in the middle of the D_{Max} range. In the reconstructions described below, we used a 200 Å dimension. The complex of r(TSA$_0$)/drd(BS) with p20 shares a similar D_{Max} range (195−200 Å) and similar R_g values (Table 2) as free r(TSA$_0$)/drd(BS) alone, with a similar overall shape of the $p(r)$ curve

dx.doi.org/10.1021/bi300935p | *Biochemistry* 2012, 51, 9312−9322

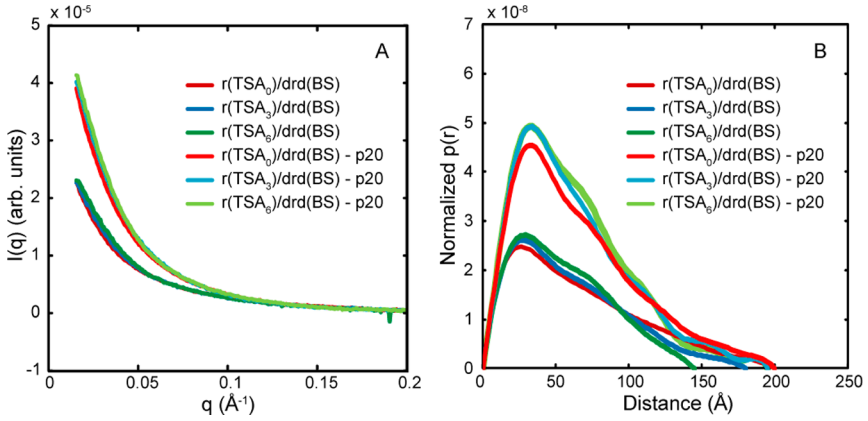

Figure 5. Scattering profiles and $p(r)$ for r(TSA$_0$-A$_6$)/drd(BS), and their complexes with p20. (A) Scattering profiles of the hybrid duplexes alone and in their respective complexes with p20. A log−log plot of these data is provided in Figure S6 of the Supporting Information. (B) $p(r)$ plots for hybrid duplexes and their complexes. Note that D_{Max} values for r(TSA$_0$)/drd(BS) and its complex are equivalent, suggesting no global change in the conformation of the duplex. However, for both r(TSA$_3$)/drd(BS) and r(TSA$_6$)/drd(BS), the D_{Max} increases upon complex formation to a D_{Max} similar to that of the r(TSA$_0$)/drd(BS)−p20 complex [note that at distances near 200 Å the curve for the r(TSA$_6$)/drd(BS)−p20 complex lies immediately below that for the A$_0$ and A$_3$ complexes and is obscured from view].

(Figure 4, green and blue curves). These similarities indicate that p20 does not induce a detectable conformational change of perfect dsRNA on the global scale.

Data were also collected for the bulged chimeric duplexes, r(TSA$_3$)/drd(BS) and r(TSA$_6$)/drd(BS), and their respective complexes (Figure 5). Because bulges are known to induce bends in dsRNA,[34,35,43,44] these complexes offered the potential to test for conformational changes induced by the dsRBD. We note that the concentrations of duplex and p20 used to form the complexes do suggest some amount of nonspecific binding (Figure 1), which precludes a full structural analysis. Nonetheless, SAXS analysis of the data could still be conducted: chimeric duplexes are the major component of the scattering curves and thus dominate the $p(r)$ scattering curve (Figure 4B). Therefore, observed changes in the $p(r)$ and D_{Max} of the bulged duplexes upon binding qualitatively suggest changes in the global conformation of the duplex.

For r(TSA$_3$)/drd(BS) and r(TSA$_6$)/drd(BS), the observed D_{Max} values are 180 and 145 Å, respectively (Figure 5). Zacharias and Hagerman used transient electric birefringence (TEB) to measure bulge-induced bend angles for A$_0$, A$_3$, and A$_6$ bulges in dsRNA of 0°, 58 ± 4°, and 93 ± 3°, respectively.[35] Using triangulation, we calculate end-to-end distances of 175 ± 3 and 138 ± 3 Å for r(TSA$_3$)/drd(BS) and r(TSA$_6$)/drd(BS), respectively. The TEB-predicted value of 175 ± 3 Å for r(TSA$_3$)/drd(BS) is in good agreement with the SAXS D_{Max} value of 180 Å, and the TEB-predicted value of 138 ± 3 Å for r(TSA$_6$)/drd(BS) is in good agreement with the smaller SAXS D_{Max} value of 145 Å. Thus, the correct trends of D_{Max} with bulge size are found by SAXS.

For r(TSA$_3$)/drd(BS) and r(TSA$_6$)/drd(BS), the D_{Max} values of 180 and 145 Å change to ∼195 Å upon binding of p20, which is within the range of the values of r(TSA$_0$)/drd(BS) and its complex (Figure 5). This change in the global dimension of the bulged duplexes to that of the perfect duplex upon complex formation supports the observation that p20 straightens the bulge-induced bends in the duplex.

As revealed in Figure 5, as the bulge size increases, the shoulders (features) in $p(r)$ become more pronounced and extend to slightly higher distances compared to those in the perfect duplex. The increased magnitude of the shoulders with bulge size likely indicates contributions of the extra bulged nucleotides and their arrangements relative to the rest of the structure: even when straightened, the bulge nucleotides likely adopt a conformation different from that of the hybrid extensions. In addition, the duplexes with the bulges have a slightly greater contribution to $p(r)$ (than the unbulged duplex) at intermediate distances of 50−100 Å and slightly smaller contributions to $p(r)$ (than the unbulged duplex) at 150−200 Å (Figure 5B); this may indicate that in the bulged duplexes there are contributions of states that are not fully extended either due to dynamics or due to incomplete straightening. This is also reflected in somewhat smaller R_g values for the complexes with the bulged duplexes (Table 2). Nonetheless, observation that the D_{Max} values are nearly identical for unbulged and A$_3$- and A$_6$-bulged complexes supports the idea that the bulged duplexes are largely straightened.

SAXS Reconstructions of r(TSA0)/drd(BS) and p20, Alone and in a Complex. In this section, we consider reconstructions of p20, r(TSA$_0$)/drd(BS), and their complex. The *GNOM* outputs for p20 and r(TSA$_0$)/drd(BS) were then used as *DAMMIF* inputs to generate structural models of the protein and duplex alone (see Materials and Methods). The outputs of multiple *DAMMIF*[29] runs were then aligned, averaged, and filtered via volume constraints using *DAMAVER*[31] (see Materials and Methods).

First, we consider reconstruction of p20 alone. Figure 6 shows the reconstruction (gray envelope) of the p20 data from 10 *DAMMIF* runs (fast mode) with an MNSD of 0.720 ± 0.017, overlaid on the best representative NMR conformer of p20 identified in the original study (orange ribbon).[40] *DAMAVER* was also used to calculate an average model structure using all conformers from the NMR study (blue envelope). Both the best representative conformer and the average model fit well within the reconstruction. The SAXS reconstruction does not speak directly to the exact conformation of the flexible linker, as the density between the two binding domains could accommodate multiple conformations. However, the reconstruction does provide information about the general orientation and spatial relationship of the binding domains.

dx.doi.org/10.1021/bi300935p | *Biochemistry* 2012, 51, 9312−9322

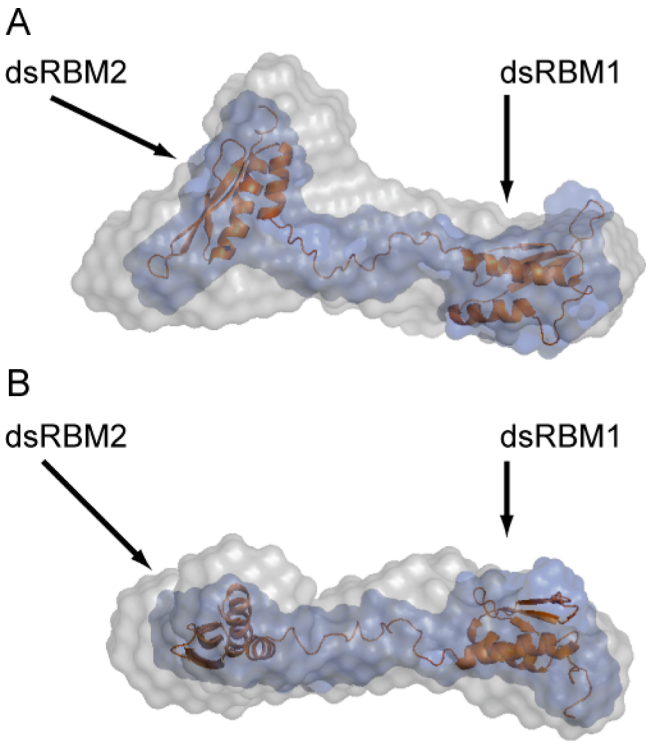

Figure 6. SAXS reconstruction of p20 overlaid on the NMR structure (Protein Data Bank entry 1QU6). (A) Front view of the best representative conformer of an NMR structure of p20 (orange ribbon) and a space-filling model of the average NMR structure (blue envelope) calculated using *DAMAVER* overlaid with the molecular envelope (gray envelope) generated from SAXS scattering curves. (B) Top-down view of the structure in panel A.

Next, we consider reconstruction of the perfect chimeric duplex alone. Reconstruction of r(TSA_0)/drd(BS) alone with an MNSD of 0.608 ± 0.022 is provided in Figure S4 of the Supporting Information, overlaid with a hybrid duplex model generated in pieces using the Nucleic Acid Builder Web Server.[45] The model was generated using two 22 bp B-form hybrid helices (green) and one 16 bp A-form RNA helix. The transition region between the two types of duplexes was modeled with structural properties intermediate between those of the A- and B-forms, which yielded a D_{max} consistent with the data. Interestingly, this gives the hybrid a smooth, curved shape that is very similar to that of the molecular envelope (Figure S4 of the Supporting Information). Also, the transition points in the envelope match well with the transition points between the different helical forms. This shape of r(TSA_0)/drd(BS) is also supported by NMR studies of a similar chimeric duplex, which were consistent with a bend.[46]

Finally, reconstructions of the r(TSA_0)/drd(BS) complex were performed (Figure 7). We used *MONSA*,[30] which generates models of the complex that differentiate between nucleic acid and protein components. To efficiently model the complex from the *MONSA* output, 10 reconstructions were averaged, with an MNSD of 0.626 ± 0.044 showing that the individual complexes agreed well with each other. However, as *DAMAVER* does not retain information about the relative placement of the proteins and nucleic acid components, the average density of the nucleic acid alone from the complexes was used to guide placement of the hybrid model within the SAXS envelope, which is shown in Figure 7. The curved hybrid, which is already present in the uncomplexed chimeric duplex (Figure S4 of the Supporting Information), is accommodated well by the envelope, suggesting that the binding of p20 does not globally deform the structure. Furthermore, a model of p20 is readily docked within the excess volume of the envelope

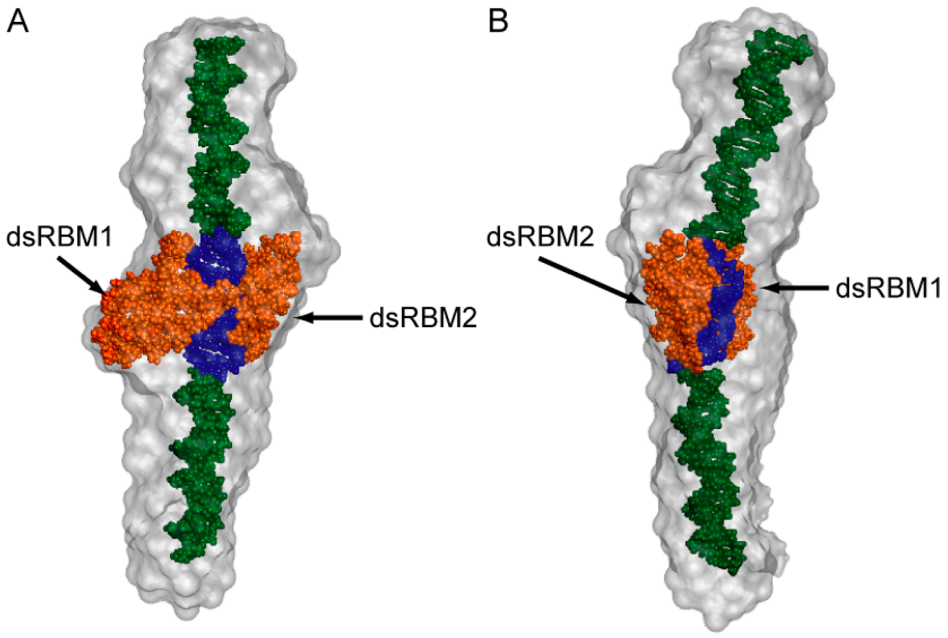

Figure 7. SAXS reconstruction of the r(TSA_0)/drd(BS) complex with the docked bound model. (A) Front and (B) side views of the model, with the SAXS envelope colored gray and the A-form helix, B-form helices, and p20 protein colored blue, green, and orange, respectively. These two views are related by an ~90° clockwise rotation about the vertical axis. See the text for details about the construction of the model. Note that the curved structure of the hybrid is matched by the slight curving through the SAXS envelope and is present in the free chimeric duplex (Figure S4 of the Supporting Information).

dx.doi.org/10.1021/bi300935p | *Biochemistry* 2012, 51, 9312–9322

surrounding the A-form portion of the hybrid model. This bound version of p20 was obtained by rotating the binding domains to interact with the minor groove[7] and reorganizing the linker to run through the A-form major groove to generally replicate the bound model.[47] The p20 model fits reasonably into the density, although there is some unmodeled density just above dsRBM2 (Figure 7A, right), which suggests that the grooves in the hybrid may actually be shifted slightly higher than modeled because of the intermediate nature of the helical forms. However, excellent agreement is achieved overall between the model and the SAXS envelope, supporting binding of p20 to only the dsRNA portion of the chimera without alteration of the global conformation of the hybrid.

DISCUSSION

In this study, we investigated the interaction between the dsRBD of PKR and chimeric duplexes having a dsRNA segment and flanking RNA−DNA hybrid regions. EMSAs suggested specific, tight binding to the perfect dsRNA segment based on a well-resolved shift, and weak nonspecific binding to bulged dsRNAs and RNA−DNA hybrids based on a smear. ITC experiments were able to quantify the thermodynamic basis for dsRBM−RNA specificity. There is ∼66−166-fold tighter binding to the perfect site versus the bulged and RNA−DNA hybrid sites. Also, there is a single specific site for the dsRNA portion versus approximately three or four nonspecific sites for the hybrid portion. Binding is enthalpically driven, with values in reasonable agreement with van't Hoff parameters from prior EMSA studies.[25] The number of nonspecific sites determined for the various duplexes correlates with the number of sites expected from prior studies on dsRNA and with general statistical effects for saturating a large non-sequence-specific lattice.[37]

Binding of bulged RNAs relative to perfect RNAs at 20 °C was weaker than previously reported (∼66-fold weakening here vs 2.3-fold seen previously);[25] this is also revealed in the nature of the gel shifts, which are smeared here but were resolved previously.[25] The major difference between these two studies is use of a 16 bp dsRNA site here, versus a 22 bp site previously; the former site gives rise to one gel shift and the latter to two,[7] which suggests that a bulge is more penalizing in the context of a smaller dsRNA segment. Given that most cellular RNAs have short helical regions, this suggests that bulges are quite detrimental to PKR binding in vivo. Notably, this is suggestive of structural specificity in the dsRBM, despite no sequence specificity.

SAXS experiments provided scattering profiles and reconstructions for p20, r(TSA$_0$)/drd(BS), and their complex that were consistent with little or no conformational change. In contrast, $p(r)$ plots for the A$_3$- and A$_6$-bulged chimeric duplexes suggested conformational changes in the duplex consistent with straightening of the bulged dsRNA segment back to an A-form-like geometry. This result indicates that the dsRBD prefers A-form substrates and can even bind and straighten non-A-form (e.g., bent) RNAs of adequate length and flexibility. This result is consistent with crystal structures of dsRBM−dsRNA complexes from Xlrbpa-2 and Aa-RNase III in which the bound RNA is A-form, or nearly A-form,[8,48] as well as an earlier qualitative study of p20 using EMSAs.[25]

PKR's ability to discriminate against most RNAs containing imperfections, especially smaller RNAs, suggests that more complex RNAs interact with PKR either by mimicking dsRNA, as recently reported for HCV domain II[19] and pseudoknots,[16,20] or by engaging portions of PKR outside of the dsRBD. Modeling of helical RNAs suggests that many non-Watson−Crick regions can fold into A-form-like geometries.[49] This would increase the range of RNA substrates with which PKR and other dsRBD-containing proteins can interact.

One important finding of this study is that PKR interacts with RNAs containing imperfections and with RNA−DNA hybrids, albeit ∼200-fold more weakly. Weak binding of PKR to RNA with imperfections and to RNA−DNA hybrids suggests that in a noninfected cell PKR may interact with abundant RNAs with imperfections, which may become straightened; this would be consistent with reports that PKR interacts with rRNA via its dsRBD.[50] Such structured RNAs may avoid activation of PKR by either being too short to assemble the two protomers in proper juxtaposition or by titrating PKR monomers out to separate RNAs. These weak, nonproductive interactions may buffer PKR in its latent state until an activating RNA provokes an immune response.

ASSOCIATED CONTENT

Supporting Information

Binding of p20 to chimeric duplexes in the presence of BSA and herring sperm DNA by EMSAs, binding of p20 to the perfect chimeric duplex r(TSA$_0$)/p*drd(BS) by EMSAs at low temperatures, binding of p20 to bulged chimeric duplex r(TSA$_6$)/p*drd(BS) by EMSAs at low temperatures, SAXS reconstruction of r(TSA$_0$)/drd(BS), and log−log plots of SAXS data. This material is available free of charge via the Internet at http://pubs.acs.org.

AUTHOR INFORMATION

Corresponding Author

*P.C.B.: phone, (814) 863-3812; e-mail, pcb5@psu.edu. L.P.: phone, (607) 255-8695; e-mail, lp26@cornell.edu.

Present Address

[§]Department of Biochemistry and Molecular Biophysics, Washington University School of Medicine in St. Louis, St. Louis, MO 63110.

Author Contributions

S.P. and J.M.B. contributed equally to this work.

Funding

This work was supported by National Institutes of Health Grants GM-058709 to P.C.B., GM-088645 to L.P., and 1F31NS054492-01 to J.E.S., as well as by National Science Foundation (NSF) Grant MRI 0922974 for support of the Penn State Automated Biological Calorimetry Facility. CHESS is supported by the NSF and the National Institute of General Medical Sciences via NSF Grant DMR-0936384.

Notes

The authors declare no competing financial interest.

ACKNOWLEDGMENTS

We thank Saikat Ghosh, Chelsea Hull, and Scott Showalter for comments on the manuscript and Subba Rao Nallagatla for helpful conversations. We also thank Steve Meisburger and Suzette Pabit for their assistance in collecting SAXS data.

ABBREVIATIONS

dsRNA, double-stranded RNA; dsRBD, dsRNA-binding domain; dsRBM, dsRNA binding motif; EMSA, electrophoretic mobility shift assay; ITC, isothermal titration calorimetry; PKR,

RNA-activated protein kinase; p20, dsRBD from PKR; SAXS, small-angle X-ray scattering.

REFERENCES

(1) Garcia, M. A., Meurs, E. F., and Esteban, M. (2007) The dsRNA protein kinase PKR: Virus and cell control. *Biochimie 89*, 799−811.

(2) Manche, L., Green, S. R., Schmedt, C., and Mathews, M. B. (1992) Interactions between double-stranded RNA regulators and the protein kinase DAI. *Mol. Cell. Biol. 12*, 5238−5248.

(3) Zheng, X., and Bevilacqua, P. C. (2004) Activation of the protein kinase PKR by short double-stranded RNAs with single-stranded tails. *RNA 10*, 1934−1945.

(4) St Johnston, D., Brown, N. H., Gall, J. G., and Jantsch, M. (1992) A conserved double-stranded RNA-binding domain. *Proc. Natl. Acad. Sci. U.S.A. 89*, 10979−10983.

(5) Tian, B., Bevilacqua, P. C., Diegelman-Parente, A., and Mathews, M. B. (2004) The double-stranded-RNA-binding motif: Interference and much more. *Nat. Rev. Mol. Cell Biol. 5*, 1013−1023.

(6) Chang, K. Y., and Ramos, A. (2005) The double-stranded RNA-binding motif, a versatile macromolecular docking platform. *FEBS J. 272*, 2109−2117.

(7) Bevilacqua, P. C., and Cech, T. R. (1996) Minor-groove recognition of double-stranded RNA by the double-stranded RNA-binding domain from the RNA-activated protein kinase PKR. *Biochemistry 35*, 9983−9994.

(8) Ryter, J. M., and Schultz, S. C. (1998) Molecular basis of double-stranded RNA-protein interactions: Structure of a dsRNA-binding domain complexed with dsRNA. *EMBO J. 17*, 7505−7513.

(9) Nallagatla, S. R., and Bevilacqua, P. C. (2008) Nucleoside modifications modulate activation of the protein kinase PKR in an RNA structure-specific manner. *RNA 14*, 1201−1213.

(10) Goodman, R. A., Macbeth, M. R., and Beal, P. A. (2012) ADAR proteins: Structure and catalytic mechanism. *Curr. Top. Microbiol. Immunol. 353*, 1−33.

(11) Hundley, H. A., and Bass, B. L. (2010) ADAR editing in double-stranded UTRs and other noncoding RNA sequences. *Trends Biochem. Sci. 35*, 377−383.

(12) Kim, Y. K., Furic, L., Desgroseillers, L., and Maquat, L. E. (2005) Mammalian Staufen1 recruits Upf1 to specific mRNA 3′UTRs so as to elicit mRNA decay. *Cell 120*, 195−208.

(13) Martel, C., Dugre-Brisson, S., Boulay, K., Breton, B., Lapointe, G., Armando, S., Trepanier, V., Duchaine, T., Bouvier, M., and Desgroseillers, L. (2010) Multimerization of Staufen1 in live cells. *RNA 16*, 585−597.

(14) Han, J., Lee, Y., Yeom, K. H., Nam, J. W., Heo, I., Rhee, J. K., Sohn, S. Y., Cho, Y., Zhang, B. T., and Kim, V. N. (2006) Molecular basis for the recognition of primary microRNAs by the Drosha-DGCR8 complex. *Cell 125*, 887−901.

(15) Nallagatla, S. R., Toroney, R., and Bevilacqua, P. C. (2011) Regulation of innate immunity through RNA structure and the protein kinase PKR. *Curr. Opin. Struct. Biol. 21*, 119−127.

(16) Cohen-Chalamish, S., Hasson, A., Weinberg, D., Namer, L. S., Banai, Y., Osman, F., and Kaempfer, R. (2009) Dynamic refolding of IFN-γ mRNA enables it to function as PKR activator and translation template. *Nat. Chem. Biol. 5*, 896−903.

(17) Nallagatla, S. R., Hwang, J., Toroney, R., Zheng, X., Cameron, C. E., and Bevilacqua, P. C. (2007) 5′-Triphosphate-dependent activation of PKR by RNAs with short stem-loops. *Science 318*, 1455−1458.

(18) Heinicke, L. A., Wong, C. J., Lary, J., Nallagatla, S. R., Diegelman-Parente, A., Zheng, X., Cole, J. L., and Bevilacqua, P. C. (2009) RNA dimerization promotes PKR dimerization and activation. *J. Mol. Biol. 390*, 319−338.

(19) Toroney, R., Nallagatla, S. R., Boyer, J. A., Cameron, C. E., and Bevilacqua, P. C. (2010) Regulation of PKR by HCV IRES RNA: Importance of domain II and NS5A. *J. Mol. Biol. 400*, 393−412.

(20) Ben-Asouli, Y., Banai, Y., Pel-Or, Y., Shir, A., and Kaempfer, R. (2002) Human interferon-γ mRNA autoregulates its translation through a pseudoknot that activates the interferon-inducible protein kinase PKR. *Cell 108*, 221−232.

(21) McKenna, S. A., Lindhout, D. A., Shimoike, T., Aitken, C. E., and Puglisi, J. D. (2007) Viral dsRNA inhibitors prevent self-association and autophosphorylation of PKR. *J. Mol. Biol. 372*, 103−113.

(22) Wahid, A. M., Coventry, V. K., and Conn, G. L. (2009) The PKR-binding domain of adenovirus VA RNAI exists as a mixture of two functionally non-equivalent structures. *Nucleic Acids Res. 37*, 5830−5837.

(23) Launer-Felty, K., Wong, C. J., Wahid, A. M., Conn, G. L., and Cole, J. L. (2010) Magnesium-dependent interaction of PKR with adenovirus VAI RNA. *J. Mol. Biol. 402*, 638−644.

(24) Heinicke, L. A., Nallagatla, S. R., Hull, C. M., and Bevilacqua, P. C. (2011) RNA helical imperfections regulate activation of the protein kinase PKR: Effects of bulge position, size, and geometry. *RNA 17*, 957−966.

(25) Zheng, X., and Bevilacqua, P. C. (2000) Straightening of bulged RNA by the double-stranded RNA-binding domain from the protein kinase PKR. *Proc. Natl. Acad. Sci. U.S.A. 97*, 14162−14167.

(26) Nielsen, S. S., Moller, M., and Gillilan, R. E. (2012) High-throughput biological small-angle X-ray scattering with a robotically loaded capillary cell. *J. Appl. Crystallogr. 45*, 213−223.

(27) Tate, M. W., Eikenberry, E. F., Barna, S. L., Wall, M. E., Lowrance, J. L., and Gruner, S. M. (1995) A large-format high-resolution area X-ray detector based on a fiber-optically bonded charge-coupled device (CCD). *J. Appl. Crystallogr. 28*, 196−205.

(28) Svergun, D. I. (1992) Determination of the regularization parameter in indirect-transform methods using perceptual criteria. *J. Appl. Crystallogr. 25*, 495−503.

(29) Franke, D., and Svergun, D. I. (2009) DAMMIF, a program for rapid ab-initio shape determination in small-angle scattering. *J. Appl. Crystallogr. 42*, 342−346.

(30) Svergun, D. I. (1999) Restoring low resolution structure of biological macromolecules from solution scattering using simulated annealing. *Biophys. J. 76*, 2879−2886.

(31) Volkov, V. V., and Svergun, D. I. (2003) Uniqueness of ab initio shape determination in small-angle scattering. *J. Appl. Crystallogr. 36*, 860−864.

(32) Kozin, M. B., and Svergun, D. I. (2001) Automated matching of high- and low-resolution structural models. *J. Appl. Crystallogr. 34*, 33−41.

(33) DeLano, W. L. (2002) *The PyMOL molecular graphics system*, DeLano Scientific, San Carlos, CA.

(34) Bhattacharyya, A., Murchie, A. I. H., and Lilley, D. M. J. (1990) RNA bulges and the helical periodicity of double-stranded RNA. *Nature 343*, 484−487.

(35) Zacharias, M., and Hagerman, P. J. (1995) Bulge-induced bends in RNA: Quantification by transient electric birefringence. *J. Mol. Biol. 247*, 486−500.

(36) Williams, B. R. (1999) PKR; a sentinel kinase for cellular stress. *Oncogene 18*, 6112−6120.

(37) McGhee, J. D., and von Hippel, P. H. (1974) Theoretical aspects of DNA-protein interactions: Co-operative and non-co-operative binding of large ligands to a one-dimensional homogeneous lattice. *J. Mol. Biol. 86*, 469−489.

(38) Bass, B. L., Hurst, S. R., and Singer, J. D. (1994) Binding properties of newly identified *Xenopus* proteins containing dsRNA-binding motifs. *Curr. Biol. 4*, 301−314.

(39) VanOudenhove, J., Anderson, E., Krueger, S., and Cole, J. L. (2009) Analysis of PKR structure by small-angle scattering. *J. Mol. Biol. 387*, 910−920.

(40) Nanduri, S., Carpick, B. W., Yang, Y., Williams, B. R., and Qin, J. (1998) Structure of the double-stranded RNA-binding domain of the protein kinase PKR reveals the molecular basis of its dsRNA-mediated activation. *EMBO J. 17*, 5458−5465.

(41) Zimmerman, S. B., and Pheiffer, B. H. (1981) A RNA·DNA hybrid that can adopt two conformations: An X-ray diffraction study of

poly(rA)·poly(dT) in concentrated solution or in fibers. *Proc. Natl. Acad. Sci. U.S.A. 78*, 78−82.
(42) Romainczyk, O., Endeward, B., Prisner, T. F., and Engels, J. W. (2011) The RNA-DNA hybrid structure determined by EPR, CD and RNase H1. *Mol. Biosyst. 7*, 1050−1052.
(43) Tang, R. S., and Draper, D. E. (1990) Bulge loops used to measure the helical twist of RNA in solution. *Biochemistry 29*, 5232−5237.
(44) Riordan, F. A., Bhattacharyya, A., McAteer, S., and Lilley, D. M. (1992) Kinking of RNA helices by bulged bases, and the structure of the human immunodeficiency virus transactivator response element. *J. Mol. Biol. 226*, 305−310.
(45) Stroud, J. (2012) Make-na webserver (Nucleic Acid Builder).
(46) Szyperski, T., Gotte, M., Billeter, M., Perola, E., Cellai, L., Heumann, H., and Wuthrich, K. (1999) NMR structure of the chimeric hybrid duplex r(gcaguggc)·r(gcca)d(CTGC) comprising the tRNA-DNA junction formed during initiation of HIV-1 reverse transcription. *J. Biomol. NMR 13*, 343−355.
(47) Nanduri, S., Rahman, F., Williams, B. R., and Qin, J. (2000) A dynamically tuned double-stranded RNA binding mechanism for the activation of antiviral kinase PKR. *EMBO J. 19*, 5567−5574.
(48) Blaszczyk, J., Gan, J., Tropea, J. E., Court, D. L., Waugh, D. S., and Ji, X. (2004) Noncatalytic assembly of ribonuclease III with double-stranded RNA. *Structure 12*, 457−466.
(49) Parisien, M., and Major, F. (2008) The MC-Fold and MC-Sym pipeline infers RNA structure from sequence data. *Nature 452*, 51−55.
(50) Zhu, S., Romano, P. R., and Wek, R. C. (1997) Ribosome targeting of PKR is mediated by two double-stranded RNA-binding domains and facilitates *in vivo* phosphorylation of eukaryotic initiation factor-2. *J. Biol. Chem. 272*, 14434−14441.